Topological Signatures of Heating and Dark Matter in the 21 cm Forest

Hayato Shimabukuro

South-Western Institute for Astronomy Research (SWIFAR),
Yunnan University, Kunming, Yunnan 650500, People's Republic of China
Key Laboratory of Survey Science of Yunnan Province,
Yunnan University, Kunming, Yunnan 650500, People's Republic of China
Graduate School of Science, Division of Particle and Astrophysical Science,
Nagoya University, Chikusa-Ku, Nagoya, 464-8602, Japan*
(Dated: November 18, 2025)

We show that the topology of the 21 cm forest carries cosmological information that is inaccessible to traditional amplitude- or correlation-based statistics. Applying topological data analysis to simulated spectra covering a range of X-ray heating efficiencies and dark-matter free-streaming scales, we compute persistence diagrams and Betti-0 curves that describe the formation and merger hierarchy of absorption troughs. A small set of interpretable descriptors—trough-line density, lifetime variance, and lifetime skewness—respond in nearly orthogonal directions across the $(f_X, m_{\rm WDM})$ plane, enabling a substantial reduction of the degeneracy between heating and dark-matter suppression. These topological signatures remain detectable under SKA1-Low-like thermal noise, demonstrating that topology provides a stable and non-Gaussian probe of small-scale physics during Cosmic Dawn.

I. INTRODUCTION

The 21 cm forest consists of narrow absorption features imprinted on the spectra of high-redshift radio sources by neutral hydrogen during the Cosmic Dawn and the epoch of reionization [1–5]. Each feature probes the optical depth

$$\tau_{\nu} = \frac{3h_{p}c^{3}A_{10}}{32\pi^{3/2}k_{B}\nu_{21}^{2}} \int \frac{n_{\rm HI}(x)}{b(x)T_{S}(x)} \exp\left[-\frac{(u(\nu) - v(x))^{2}}{b^{2}(x)}\right] dx,$$
(1)

where $n_{\rm HI}$ is the neutral-hydrogen density, T_S the spin temperature, $b=(2k_BT_K/m_H)^{1/2}$ the Doppler parameter, and v(x) the line-of-sight velocity. For $\tau_{\nu}\ll 1$, the corresponding differential brightness temperature relative to the background radiation T_{γ} is

$$\delta T_b(\hat{s}, \nu) \approx \frac{T_S(\hat{s}, z) - T_{\gamma}(\hat{s}, z)}{1 + z} \tau(\hat{s}, z), \tag{2}$$

which directly connects the thermal and kinematic state of the IGM to the observed absorption profile. Here, \hat{s} denotes the unit vector along the line of sight (i.e., the observing direction), ν is the observed frequency corresponding to redshift $z = \nu_{21}/\nu - 1$, T_S is the spin temperature of neutral hydrogen, T_{γ} is the brightness temperature of the background radiation (set by the flux of the radio source or the CMB), and $\tau(\hat{s}, z)$ is the optical depth along the same direction.

The 21 cm forest has emerged as a promising probe for exploring both cosmology and astrophysics, enabling tests of dark-matter models and intergalactic heating processes through absorption spectra of high-redshift radio sources [6–16]. These studies demonstrate that the morphology and amplitude of the 21 cm absorption pattern are jointly shaped by the microscopic properties of dark matter and by astrophysical heating, particularly from X-rays. A major challenge is therefore to disentangle the imprint of dark-matter free streaming from that of X-ray heating, since both influence the small-scale structure and thermal evolution of the intergalactic medium in similar ways. Variations in the X-ray efficiency f_X and in alternative dark-matter models (e.g., WDM or axion-like ultralight dark matter) produce degenerate effects in conventional amplitude-based analyses of the forest.

The one-dimensional power spectrum of the 21 cm forest is a key probe of small-scale physics but captures only second-order moments [16–19]. The wavelet scattering transform (WST) extends this to nonlinear couplings and higher-order correlations[20, 21]. Despite its success in recent applications to the Lyman- α and 21 cm forests, the WST does not directly quantify the geometric connectivity or topology of absorption troughs. It characterizes the strength of fluctuations but not their morphological organization. Morphological and topological analyses using Minkowski functionals have been applied to the 21 cm brightness field [22–28], revealing non-Gaussian structural evolution during reionization.

Here we propose topological data analysis (TDA) as a complementary framework that extends beyond amplitude- and correlation-based statistics such as the power spectrum and WST [29–31]. By constructing one–dimensional sublevel filtrations of δT_b and tracking births and mergers of connected components, we obtain persistence diagrams and Betti curves that characterize how troughs emerge and coalesce across thresholds. Topological descriptors are invariant under smooth (monotonic) transformations and intrinsically sensitive to non–Gaussian morphology; TDA has been fruitfully applied across cosmology, from the cosmic web and lensing to reionization topology [32–38]. Unlike power spectra that encode only second-order moments, topology is

^{*}Electronic address: shimabukuro@ynu.edu.cn

sensitive to the rank-ordering of extrema and therefore captures phase correlations neglected by conventional statistics.

The formalism developed here is generic and can be applied beyond the 21 cm forest (e.g., to 21 cm tomography and the Lyman- α forest). Using persistence diagrams, lifetime statistics, and Betti-0 curves, we uncover distinct, interpretable topological signatures of models that vary in X-ray heating efficiency f_X and dark-matter mass $m_{\rm DM}$. In particular, the trough line density, the lifetime second moment, and the lifetime skewness respond along complementary directions in (f_X, m_{DM}) , respectively tracing small-scale suppression, contrast compression, and morphological asymmetry. These topologybased summaries are invariant under smooth rescalings, remain informative in the presence of realistic thermal noise, and complement power-spectrum and WST analyses. Together, these properties allow clearer model separation even in regimes where amplitude- or correlationbased measures appear nearly degenerate.

II. METHOD

The one-dimensional 21 cm forest spectra analyzed in this work are taken from the semi-numerical simulations of Ref. [18], produced for both cold and warm dark matter models and a range of X-ray heating efficiencies f_X . We focus on the epoch at redshift z=9, where the intergalactic medium remains largely neutral and the 21 cm absorption signal is most pronounced. We analyze ten independent lines of sight per model, each spanning $10\,\mathrm{cMpc}$, with $1\,\mathrm{kHz}$, corresponding to the expected channel width of the SKA1-Low observations[39]. 10 independent lines of sight are motivated by theoretical predictions that approximately twenty bright radio quasars are expected to exist at $z\simeq 9$ in forthcoming surveys, making this sample size representative of realistic observational prospects[40].

Each spectrum $x(\nu)$ is lightly detrended and standardized prior to the topological analysis. Specifically, we apply a Z-score normalization,

$$z(\nu) = \frac{x(\nu) - \langle x \rangle}{\sigma_x},\tag{3}$$

where $\langle x \rangle$ and σ_x are the mean and standard deviation of the brightness temperature along each line of sight. We standardize each spectrum to remove amplitude dependence and place all models on a common dimensionless threshold scale.

III. TOPOLOGICAL FORMALISM

For a one-dimensional field $z(\nu)$, the sublevel set at threshold t is

$$X_t = \{ \nu \mid z(\nu) < t \}.$$
 (4)

Physically, this corresponds to progressively revealing structures from the deepest absorption troughs to shallower ones by lowering a brightness–temperature threshold. The 'birth' of a component marks the appearance of a new trough, while its 'death' captures the moment it merges with an adjacent, deeper one and becomes indistinguishable. As t increases, individual absorption troughs emerge and merge, forming a topology characterized by the homology group H_0 . Each connected component is born at threshold b_j and dies at d_j when it merges with an older one. The set of birth–death pairs (b_j, d_j) defines the persistence diagram (PD), and the persistence lifetime $\tau_j = d_j - b_j$ quantifies the prominence of each trough. The number of components alive at threshold t gives the Betti–0 curve,

$$\beta_0(t) = \#\{j \mid b_j \le t < d_j\} \tag{5}$$

Betti-0 counts distinct absorption systems, and their persistence lifetimes trace the depth hierarchy of potential wells in the IGM.

From the PD we retain long-lived features using a common persistence cut $\tau_{\star} = 0.411$. This value is chosen as the 95th percentile of the baseline model to exclude numerical short-lived features; alternative cuts yield consistent qualitative trends, and define the set $\mathcal{I}_{\text{long}} = \{j : \tau_j \geq \tau_{\star}\}$. Unless stated otherwise, the intensity threshold t_{\star} is fixed by the peak of the noiseless CDM $\beta_0(t)$ and applied uniformly to all models (to avoid selection bias).

(i) Trough line density. For a frequency span $\Delta \nu$ at redshift z, the comoving line-of-sight length is

$$L_{\parallel} = \Delta \nu \, \frac{d\chi}{d\nu}, \qquad \frac{d\chi}{d\nu} = \frac{c(1+z)}{H(z)\,\nu_{21}}.$$
 (6)

We define the line density of absorption troughs at t_{\star} by

$$\lambda(t_{\star}) = \frac{\beta_0(t_{\star})}{L_{\parallel}} \text{ [Mpc}^{-1]}, \tag{7}$$

which primarily traces the abundance of small-scale structure (decreasing with stronger WDM suppression and with increasing X-ray heating).

(ii) Second moment of lifetimes. With $\langle \tau \rangle_{\text{long}} = \frac{1}{N_{\text{long}}} \sum_{j \in \mathcal{I}_{\text{long}}} \tau_j$, we compute

$$M_2 = \frac{1}{N_{\text{long}}} \sum_{j \in \mathcal{I}_{\text{long}}} (\tau_j - \langle \tau \rangle_{\text{long}})^2, \tag{8}$$

which captures the spread/strength of long-lived features and responds predominantly to heating-driven contrast compression.

(iii) Skewness of lifetimes. The morphological asymmetry of lifetimes is quantified by the standardized third moment

$$A_{\text{skew}} = \frac{\frac{1}{N_{\text{long}}} \sum_{j \in \mathcal{I}_{\text{long}}} (\tau_j - \langle \tau \rangle_{\text{long}})^3}{M_2^{3/2}}, \qquad (9)$$

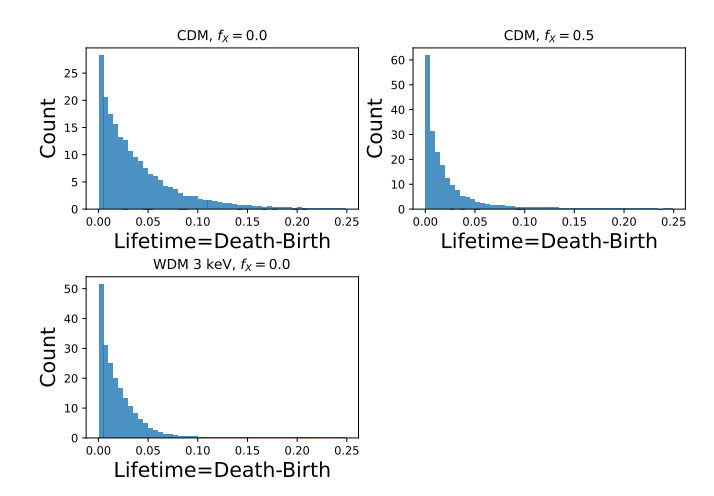


FIG. 1: Distributions of persistence lifetimes(Death-Birth) Panels compare CDM with $f_X = 0$ and 0.5 and CDM $(f_X = 0)$ versus WDM $(m_{\text{WDM}} = 3 \text{ keV}, f_X = 0)$.

which tends to flip sign between WDM- and heating-dominated regimes, providing information complementary to "how many" (λ) and "how strong" (M_2) .

IV. RESULTS

Persistence lifetime distributions.— Figure 1 compares the distributions of persistence lifetimes $\tau = d-b$ using common bins across models. For CDM, increasing f_X shifts probability toward shorter lifetimes and trims the long- τ tail, consistent with a compression of persistence caused by reduced contrast. WDM $(m_{\text{WDM}} = 3 \,\text{keV}, \, f_X = 0)$ produces an even stronger shift and a marked depletion of the tail, reflecting the removal of small-scale extrema and earlier merging of neighboring troughs. These trends anticipate the ordering of topology summaries (tail mass and the resulting count of long-lived components N_{long}) as CDM $f_X = 0$ > CDM $f_X = 0.5$ > WDM, thereby linking the lifetime statistics directly to the Betti-0 behavior.

Betti–0 curves.—Figure 2 presents the Betti–0 curves, showing the number of connected components $\beta_0(t)$ alive at threshold t for standardized brightness–temperature spectra at a spectral resolution of 1 kHz. Without persistence filtering (top panel), the raw curves include both physically meaningful structures and numerous short-lived components that arise from weak fluctuations and numerical noise. These transient features produce small oscillations and artificially broaden the $\beta_0(t)$ profiles, partially obscuring the underlying cosmological trends.

To extract only the topologically significant structures, we apply a persistence threshold of $\tau \geq 0.411$ (bottom panel), removing short-lived components while retaining the long-lived absorption troughs that reflect the IGM's physical morphology. As we have explained, the per-

sistence threshold of $\tau=0.411$ corresponds to the 95% percentile of the lifetime distribution, chosen to exclude short-lived noise-induced features while retaining physically meaningful long-lived absorption structures.

This filtering sharpens the curves and amplifies the differences between models, allowing a clearer interpretation of their topological evolution. For the unheated CDM case $(f_X = 0)$, $\beta_0(t)$ exhibits a high and broad peak, indicating numerous shallow troughs that merge gradually as t increases. Raising the X-ray heating efficiency to $f_X = 0.5$ lowers the peak and narrows the curve, reflecting the homogenization of the absorption field by heating. In contrast, warm dark matter (WDM, $3 \, \text{keV}$) yields an even smaller and sharper $\beta_0(t)$ peak, consistent with the suppression of small-scale structures and faster merging of surviving components.

Overall, the comparison between unthresholded and thresholded analyses demonstrates that persistence filtering effectively isolates the robust topological backbone of the 21 cm forest: X-ray heating compresses contrast, whereas WDM erases small-scale connectivity in the absorption landscape. The adopted 1 kHz resolution ensures that the narrow absorption features expected in SKA1-Low observations are sufficiently resolved to capture their intrinsic topological structure.

Impact of observational effects.— We investigate how the spectral resolution and thermal noise affect the topology of the 21 cm forest in the fiducial CDM model with $f_X = 0$, as summarized in Figure 3. We apply the same analysis pipeline to all spectra, consisting of detrending, per-LOS standardization, downsampling, sublevel filtration, and Betti-0 evaluation, using a fixed persistence threshold of $\tau \geq 0.411$. The left panel shows the dependence on spectral resolution in the absence of thermal noise. Coarser spectral resolution and thermal noise both reduce the number of resolved troughs, but the topological trends remain visible under SKA1-Low-like conditions (1 kHz, 1000 h).

The right panel illustrates the impact of thermal noise at 1 kHz resolution for integration times of 0 h (no noise), 100 h, and 1000 h with SKA-Low level thermal noise [39]. Thermal noise introduces numerous short-lived, shallow troughs that artificially inflate $\beta_0(t)$. Applying the same persistence threshold efficiently suppresses these spurious components, isolating the physically meaningful longlived absorption structures. As the integration time increases, the Betti-0 curve progressively converges toward the noiseless case and the line-of-sight scatter becomes smaller, demonstrating that the intrinsic topological signal of the 21 cm forest can remain detectable under realistic SKA-like noise levels. These results emphasize that preserving both fine frequency resolution and sufficiently long integration time is essential for recovering the robust topological structure of the IGM from observational 21 cm forest data.

Topological degeneracy maps. We show the signed Z-differences of the three topological descriptors $\lambda(t_{\star})$, M_2 , and A_{skew} relative to the baseline model

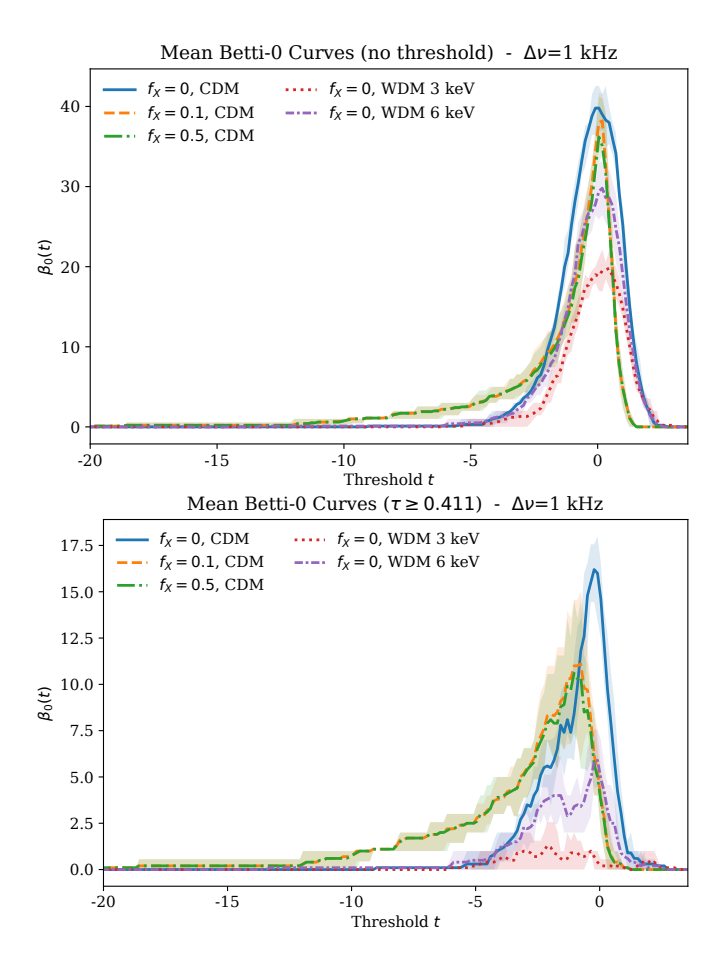


FIG. 2: **Top:** Mean Betti–0 curves $\langle \beta_0(t) \rangle$ at $\Delta \nu = 1 \, \text{kHz}$ without persistence filtering. CDM with low f_X shows a broad, high peak; stronger heating and WDM reduce small-scale troughs and hasten mergers. **Bottom:** Same, with 68% LOS bands after applying a persistence cut $\tau \geq 0.411$, which suppresses short-lived features and clarifies model differences.

(CDM, $f_X = 0$) across the $(f_X, m_{\rm DM})$ grid in Figure 4. For each point we use LOS means and dispersions, a common persistence cut $\tau_{\star} = 0.411$, and a fixed intensity threshold t_{\star} set by the noiseless CDM peak of $\beta_0(t)$; the same $(t_{\star}, \tau_{\star})$ are applied to all models and to the 1000 h thermal–noise realizations to avoid selection bias.

Three robust trends emerge. (i) The trough line density $\lambda(t_{\star})$ decreases when either f_X increases or $m_{\rm DM}$ decreases (warmer DM), reflecting the loss of small–scale absorption features from heating and free–streaming; the gradient is strongest toward the WDM direction for low–to–moderate f_X and weakens as strong heating drives the field toward noise–like behavior. (ii) The lifetime second moment M_2 primarily responds along the heating axis: increasing f_X prunes deep, long–lived troughs and compresses the lifetime distribution, reducting M_2 with only a mild dependence on $m_{\rm DM}$; under 1000 h noise the dynamic range shrinks first in the strongly heated corner. (iii) The skewness $A_{\rm skew}$ flips sign between WDM– and heating–dominated regimes, encoding a morphological asymmetry that is distinct from

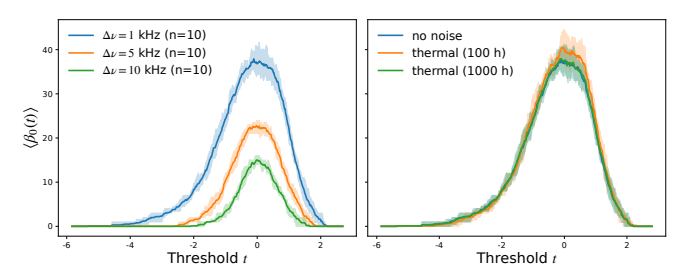


FIG. 3: **Topological sensitivity for CDM** ($f_X = 0$). A common cut $\tau \geq 0.411$ is used throughout. **Left:** Resolution dependence (1, 5, 10 kHz): coarser channels merge narrow troughs, lowering and narrowing the $\beta_0(t)$ peak. **Right:** Thermal noise at 1 kHz for 0, 100, 1000 h: longer integration suppresses noise-induced components, shrinking LOS scatter and driving the curves toward the noiseless topology.

"how many" (λ) and "how strong" (M_2); its sign structure remains discernible under noise.

These three responses probe different aspects of the signal. λ reflects the abundance of small-scale structure and is therefore sensitive to WDM. M_2 tracks the degree of contrast compression and responds mainly to the heating efficiency. $A_{\rm skew}$ provides an additional morphological discriminator through the sign of the lifetime distribution. Taken together, $\{\lambda(t_{\star}), M_2, A_{\rm skew}\}$ can therefore partially reduce the degeneracy between heating and WDM.

In practice, λ -vs- M_2 separates "structure suppression" from "contrast compression," while $A_{\rm skew}$ stabilizes the separation via its opposite–sign behavior. Although thermal noise inevitably reduces the contrast, particularly at very high f_X , the large-scale gradients in λ remain visible over most of the grid. The sign pattern in $A_{\rm skew}$ also survives in these conditions. Together, these behaviors show that the topological descriptors retain degeneracy-reducing information under realistic noise levels, and they therefore provide a useful complement to power-spectrum constraints.

V. DISCUSSION

Our results reveal a coherent but informative contrast between amplitude—based statistics and topology—based descriptors. In the power spectrum (and likewise in WST coefficients), X—ray heating suppresses power more strongly than switching to WDM. By contrast, the Betti—0 statistic $\beta_0(t)$ and the associated topological summaries decrease more markedly for WDM than for X—ray heating. Power and WST quantify "how large" fluctuations are and how scales couple, whereas $\beta_0(t)$ counts "how many" connected absorption components exist at a given threshold and in what order they merge—i.e., the topology of minima.

The physical origin of this divergence is clear. X–ray heating mainly induces a *monotonic* transformation of

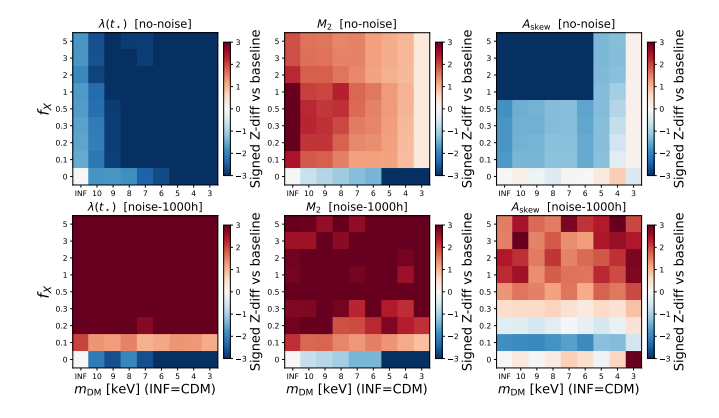


FIG. 4: Topological degeneracy maps: signed Z-difference of three descriptors relative to the baseline (CDM, f_X =0). Columns show the trough line density $\lambda(t_{\star})$, lifetime second moment M_2 , and skewness $A_{\rm skew}$; rows compare noiseless (top) and 1000 h thermal noise (bottom). Axes span X-ray heating f_X (vertical) and dark-matter mass $m_{\rm DM}$ (horizontal; INF=CDM, decreasing to 3 keV to the right). Large-scale color gradients persist under noise, especially for λ and $A_{\rm skew}$.

the brightness field: it lowers contrast but, to first order, preserves the rank ordering and spatial arrangement of troughs. Consequently, amplitude-weighted summaries such as the power spectrum and the WST decline rapidly with increasing f_X , whereas the topological summaries, which are based on rank ordering, vary much more mildly. In contrast, WDM erases small–scale perturbations through free streaming, eliminating shallow extrema and causing early merging of nearby troughs; this truncates the high– τ tail of the lifetime distribution and lowers/narrows the $\beta_0(t)$ peak, direct evidence for a simpler, more merged absorption topology.

Topological descriptors therefore, offer complementary information for inference. In particular, the three features used here respond along nearly orthogonal directions in parameter space: the line density $\lambda(t_{\star})$ tracks the abundance of small-scale structure and is most sensitive to WDM; the lifetime second moment M_2 primarily traces contrast compression by X-ray heating; and the skewness A_{skew} captures a morphological asymmetry that flips sign between heating- and WDM-dominated regimes. As shown by our degeneracy maps, combining $\{\lambda(t_{\star}), M_2, A_{\text{skew}}\}$ provides complementary constraints on $(f_X, m_{\rm DM})$ and thus has the capacity to partially disentangle their degeneracy. Importantly, these trends survive realistic observing conditions: with SKA1–Low–like thermal noise (1000 h) and $\Delta \nu = 1 \,\mathrm{kHz}$, large-scale gradients in λ and the sign structure in A_{skew} remain visible, while M_2 retains heating sensitivity except in the strongly heated, noise-like corner.

Because Betti and persistence statistics depend only on rank ordering, they are robust to smooth calibration drifts and continuum residuals. They also complement amplitude-based probes: heating reduces power yet preserves the number and hierarchy of absorption sys-

tems, while WDM leaves the opposite imprint. Combining power or WST with $\lambda, M_2, A_{\text{skew}}$ therefore enhances parameter separability beyond either class alone. There are, however, limits. At very high f_X the field approaches a noise-dominated state, and all descriptors lose contrast; in this regime the heating-WDM degeneracy necessarily tightens. Mitigations include (i) focusing on redshift/frequency ranges with stronger intrinsic contrast, (ii) increasing integration time or modestly improving spectral resolution, and (iii) applying a conservative persistence cut and a fixed, baseline-defined threshold $(\tau_{\star}, t_{\star})$ or subtracting a noise-only expectation to stabilize the metrics. Within these bounds, we find that topology provides robust, interpretable, and complementary information that strengthens cosmological inference from the 21 cm forest beyond traditional amplitude-based statistics.

VI. CONCLUSION

We show that the topology of the 21 cm forest carries independent cosmological information, enabling partial disentanglement of X-ray heating and dark-matter freestreaming effects. By tracing the birth and merger hierarchy of absorption troughs in sublevel filtrations of $\delta T_b(\nu)$, we derived persistence diagrams and Betti–0 curves that reveal the morphological organization of the intergalactic medium. The three interpretable topological descriptors $\lambda(t_\star)$, M_2 , and $A_{\rm skew}$ quantify different aspects of the morphology. $\lambda(t_\star)$ reflects the abundance of small-scale structure, M_2 measures the contrast of long-lived features, and $A_{\rm skew}$ captures the asymmetry of their lifetime distribution. Together, these descriptors complement the information provided by the power spectrum and the WST.

Across cosmological models and X-ray heating efficiencies, we find robust and physically interpretable trends: CDM yields numerous, long-lived troughs; increasing f_X compresses contrast; and WDM free-streaming suppresses small-scale connectivity. These topological signatures remain detectable under realistic observing conditions, including SKA1-Low–like noise levels for 100–1000 h of integration and a frequency resolution of $\Delta\nu=1$ kHz. This persistence shows that topology provides a stable, non-Gaussian information channel even in the presence of observational uncertainties.

Because the three descriptors respond along complementary directions in $(f_X, m_{\rm DM})$ and are invariant under smooth monotonic transformations, they add information that is both robust and orthogonal to amplitude-based statistics.

Topology thus emerges as a practical and physically transparent analysis layer for the 21 cm forest, refining our interpretation of absorption morphology and enhancing parameter separability between heating and darkmatter physics. The same topological formalism can be applied to other one-dimensional absorption fields,

providing a unified framework for non-Gaussian inference across cosmic-structure probes. Applied to high-quality data from next-generation facilities such as the SKA, topology opens a geometry-aware window onto early structure formation and the microphysics of dark matter.

No. 12103044), and Yunnan Provincial Key Laboratory of Survey Science with project No. 202449CE340002.

Acknowledgments

This work is supported by the National SKA Program of China (No.2020SKA0110401), NSFC (Grant

- [1] C. L. Carilli, N. Y. Gnedin, and F. Owen, ApJ 577, 22 (2002), astro-ph/0205169.
- [2] S. R. Furlanetto and A. Loeb, ApJ 579, 1 (2002), astroph/0206308.
- [3] S. R. Furlanetto, MNRAS 370, 1867 (2006), ISSN 0035-8711.
- [4] B. Ciardi, P. Labropoulos, A. Maselli, R. Thomas, S. Zaroubi, L. Graziani, J. S. Bolton, G. Bernardi, M. Brentjens, A. G. de Bruyn, et al., MNRAS 428, 1755 (2013), 1209.2615.
- [5] B. Ciardi, S. Inoue, K. Mack, Y. Xu, and G. Bernardi, in Advancing Astrophysics with the Square Kilometre Array (AASKA14) (2015), p. 6, 1501.04425.
- [6] Y. Xu, X. Chen, Z. Fan, H. Trac, and R. Cen, ApJ 704, 1396 (2009), 0904.4254.
- [7] Y. Xu, A. Ferrara, and X. Chen, MNRAS 410, 2025 (2011), 1009.1149.
- [8] H. Shimabukuro, K. Ichiki, S. Inoue, and S. Yokoyama, Phys. Rev. D 90, 083003 (2014), 1403.1605.
- [9] B. Semelin, MNRAS **455**, 962 (2016), 1510.02296.
- [10] H. Shimabukuro, K. Ichiki, and K. Kadota, Phys. Rev. D 101, 043516 (2020), 1910.06011.
- [11] H. Shimabukuro, K. Ichiki, and K. Kadota, Phys. Rev. D 102, 023522 (2020), 2005.05589.
- [12] T. Šoltinský, J. S. Bolton, N. Hatch, M. G. Haehnelt, L. C. Keating, G. Kulkarni, E. Puchwein, J. Chardin, and D. Aubert, MNRAS 506, 5818 (2021), 2105.02250.
- [13] M. Kawasaki, W. Nakano, H. Nakatsuka, and E. Sonomoto, J. Cosmology Astropart. Phys. 2021, 019 (2021), 2010.13504.
- [14] H. Shimabukuro, K. Ichiki, and K. Kadota, Phys. Rev. D 107, 123520 (2023), 2212.08409.
- [15] P. Villanueva-Domingo and K. Ichiki, PASJ 75, S33 (2023), 2104.10695.
- [16] Y. Shao, T.-Y. Sun, M.-L. Zhao, and X. Zhang, Phys. Rev. D 112, 063513 (2025), 2411.17094.
- [17] N. Thyagarajan, ApJ 899, 16 (2020), 2006.10070.
- [18] Y. Shao, Y. Xu, Y. Wang, W. Yang, R. Li, X. Zhang, and X. Chen, Nature Astronomy 7, 1116 (2023), 2307.04130.
- [19] T. Šoltinský, G. Kulkarni, S. P. Tendulkar, and J. S. Bolton, MNRAS 537, 364 (2025).
- [20] H. M. Tohfa, S. Bird, M.-F. Ho, M. Qezlou, and M. Fernandez, Phys. Rev. Lett. 132, 231002 (2024), 2310.06010.
- [21] H. Shimabukuro, Y. Xu, and Y. Shao, Phys. Rev. D 112, 063557 (2025), 2504.14656.
- [22] S. Yoshiura, H. Shimabukuro, K. Takahashi, and T. Matsubara, MNRAS 465, 394 (2017), 1602.02351.

- [23] S. Bag, R. Mondal, P. Sarkar, S. Bharadwaj, and V. Sahni, MNRAS 477, 1984 (2018), 1801.01116.
- [24] A. Kapahtia, P. Chingangbam, S. Appleby, and C. Park, J. Cosmology Astropart. Phys. 2018, 011 (2018), 1712.09195.
- [25] Z. Chen, Y. Xu, Y. Wang, and X. Chen, ApJ 885, 23 (2019), 1812.10333.
- [26] A. Kapahtia, P. Chingangbam, and S. Appleby, J. Cosmology Astropart. Phys. 2019, 053 (2019), 1904.06840.
- [27] A. Kapahtia, P. Chingangbam, R. Ghara, S. Appleby, and T. R. Choudhury, J. Cosmology Astropart. Phys. 2021, 026 (2021), 2101.03962.
- [28] S. K. Giri and G. Mellema, MNRAS 505, 1863 (2021), 2012.12908.
- [29] N. Otter, M. A. Porter, U. Tillmann, P. Grindrod, and H. A. Harrington, arXiv e-prints arXiv:1506.08903 (2015), 1506.08903.
- [30] L. Wasserman, arXiv e-prints arXiv:1609.08227 (2016), 1609.08227.
- [31] S. Gholizadeh and W. Zadrozny, arXiv e-prints arXiv:1809.10745 (2018), 1809.10745.
- [32] P. Pranav, H. Edelsbrunner, R. van de Weygaert, G. Vegter, M. Kerber, B. J. T. Jones, and M. Wintraecken, MN-RAS 465, 4281 (2017), 1608.04519.
- [33] W. Elbers and R. van de Weygaert, MNRAS 486, 1523 (2019), 1812.00462.
- [34] G. Wilding, K. Nevenzeel, R. van de Weygaert, G. Vegter, P. Pranav, B. J. T. Jones, K. Efstathiou, and J. Feldbrugge, MNRAS 507, 2968 (2021), 2011.12851.
- [35] S. Heydenreich, B. Brück, and J. Harnois-Déraps, A&A 648, A74 (2021), 2007.13724.
- [36] W. Elbers and R. van de Weygaert, MNRAS 520, 2709 (2023), 2209.03948.
- [37] R. Bermejo, G. Wilding, R. van de Weygaert, B. J. T. Jones, G. Vegter, and K. Efstathiou, MNRAS **529**, 4325 (2024), 2206.14655.
- [38] J. Calles, J. H. T. Yip, G. Contardo, J. Noreña, A. Rouhiainen, and G. Shiu, J. Cosmology Astropart. Phys. 2025, 064 (2025), 2412.15405.
- [39] R. Braun, A. Bonaldi, T. Bourke, E. Keane, and J. Wagg, Anticipated performance of the square kilometre array – phase 1 (ska1) (2019), 1912.12699, URL https://arxiv. org/abs/1912.12699.
- [40] Q. Niu, Y. Li, Y. Xu, H. Guo, and X. Zhang, ApJ 978, 145 (2025), 2407.18136.